Comprehensive optical diagnostics for flame behavior and soot emission response to a non-equilibrium plasma

Dandan Qi[1,2], Kaixuan Yang[1,2], Xuan Zhao[1,2], Danhua Mei[4], Yaoyao Ying[1,2], Lei Xu[1,2,3], Xin Tu[5], Dong Liu[1,2,*]

[1] *MIIT Key Laboratory of Thermal Control of Electronic Equipment, School of Energy and Power Engineering, Nanjing University of Science and Technology, Nanjing 210094, People's Republic of China.*

[2] *Advanced Combustion Laboratory, School of Energy and Power Engineering, Nanjing University of Science and Technology, Nanjing 210094, People's Republic of China.*

[3] *School of New Energy, Nanjing University of Science and Technology, Jiangyin, 214443, P.R. China*

[4] *College of Electrical Engineering and Control Science, Nanjing Tech University, Nanjing, 211816, Jiangsu, China.*

[5] *Department of Electrical Engineering and Electronics, University of Liverpool, Liverpool L69 3GJ, UK.*

[*] Corresponding author.
E-mail address: dongliu@njust.edu.cn

Abstract

This study reported comprehensive optical diagnostics for flame behavior and soot emission under directly coupling of the plasma with the flame at specific heights. The morphometric parameters of unstable flames under the direct plasma coupling were quantified. We also proposed an optical method to eliminate plasma luminescence from the field of view to extract flame intensity. At the same discharge height, with the increase of discharge frequency, the flame height decreased, while the flame horizontal extension distance and deflection angle increased. The relationships between flame morphologic and electrical parameters were obtained. The experimental results suggested a one-to-one correspondence between plasma action and flame deflection or shortening. When the plasma interacted with the flame, the overall temperature and soot emission of the flame decreased compared with that without plasma. At the same discharge height, the flame temperature and soot decreased further with the increase of discharge frequency. The soot emission changed more remarkably with the discharge frequency for higher discharge heights. With the increase of voltage, the flame temperature and soot increased at the lower discharge heights. The analysis of the experiment data demonstrated that the variation of soot emission was caused by the cooperation of multiple factors.

Keywords: optical diagnostics; non-equilibrium plasma; flame behavior; soot formation

Nomenclature

B	The collective term for the RGB value of background [-]
d	The electrode gap [mm]
d_1	Diameter of cylindrical stainless steel electrodes [mm]
d_2	Diameter of alumina ceramic tubes [mm]
f	Discharge frequency [kHz]
H	Discharge height [mm]
I	The intermittent level [-]
L	Length of the burner outlet [mm]
L_1	The length of overlap between the electrodes [mm]
$L_{f,\,0}$	Flame horizontal extension distance without plasma [mm]
$L_{f,\,p}$	Flame horizontal extension distance with plasma [mm]
N	Number of elements in a sample [-]
P	The collective term for the RGB value of plasma luminescence [-]
U	Applied voltage [kV]
W	Width of the burner outlet [mm]
X_i	The i_{th} variable
$\overline{X}$	The average value of the variable
δX_i	Uncertainty in the result
$Z_{f,\,0}$	Mean flame height above the electrodes without plasma [mm]
$Z_{f,\,T}$	Flame height from burner outlet to the bottom of electrodes [mm]
$Z_{f,\,p}$	Mean flame height above the electrodes with plasma [mm]

$Z_{f,\,h}$ Hypothetical flame height above the electrodes after the deflection [mm]

Greek symbols

η The normalized total flame height, $\eta = \frac{Z_{f,\,p}+Z_{f,\,T}}{Z_{f,\,0}+Z_{f,\,T}}$ [-]

θ Deflection of flame above electrodes with plasma [°],

$$\theta = \tan^{-1}\left(\frac{L_{f,\,p}}{Z_{f,\,p}}\right)$$

θ_0 Deflection of flame above electrodes without plasma [°],

$$\theta_0 = \tan^{-1}\left(\frac{L_{f,0}}{Z_{f,\,0}}\right)$$

σ The standard deviation of a population

1. Introduction

Combustion is the principal mode of energy conversion. However, the energy conversion efficiency of existing combustion engines is still low, and it is becoming increasingly difficult to ignore the impact of fossil fuel burning on climate change and air pollution [1]. In addition, energy conversion and utilization face severe challenges with the update of environmental systems and requirements [2, 3]. Therefore, many researchers were committed to developing new engines and fuel technologies to effectively improve engine efficiency and reduce emissions **Error! Reference source not found.**-8]. Based on such requirements, plasma-assisted combustion (PAC) had drawn extensive attention in recent years. Furthermore, extensive efforts have been made to study flame characteristics in plasma–flame interactions [9-13].

Plasma discharge can enhance combustion and control emissions via thermal, kinetic, and transport pathways due to its unique advantages in producing active species and modifying transport processes. Extensive efforts have been made to understand the emission control of plasma-assisted combustion in direct current (DC), alternating current (AC), microwave, and nanosecond discharge [14-19]. Li et al. [20] experimentally found plasma generation would increase the intensity of OH radicals' radiation when applied voltage was under a certain value. When applied voltage exceeded a certain value, the discharge stream kept increasing with the reduction of OH radicals' radiation. Cha et al. [21] suggested that the plasma could affect the soot formation process and combustion characteristics, while the flame temperature and the concentration of major species were not influenced much by the plasma generation.

This conclusion was also verified in other investigations [7]. Besides, plasma-assisted fuel oxidation was reported in Refs [22, 23] to control emissions. The results showed that the absorbance spectra of CO, CO_2, H_2O, and CH_2O appeared with the plasma discharge due to the plasma-assisted CH_4 oxidation [30]. Moreover, with the increase in discharge repetition frequency, the concentrations of CO, CO_2, and H_2O increased significantly, and the concentration of CH_4 decreased.

In terms of the active form of plasma, the studies on the direct coupling of the plasma in the flame are relatively quite limited compared with the plasma acting on the fuel or the oxidant before the combustion. To focus on the performance of the plasma-flame interaction directly, scholars carried out a series of related studies. Sun et al. [24] established a PAC system in a counterflow diffusion flame to study the direct coupling dynamic effects of plasma on flame ignition and extinction. The experimental results indicated that the active species generated by the plasma could change the chemical kinetic pathways of fuel oxidation at low temperatures. In addition, Varella et al. [25] experimentally investigated the effect of PAC on pollutant emissions of a premixed flame. The generation of free radicals and excited state substances increased, which accelerated the oxidation of CO to CO_2 and the combustion of methane. The direct coupling of the plasma with the flame was developing intensively, while the related researches for controlling emissions as soot particles were very scarce.

The flame behavior and its morphologic characteristics are also essential to estimate flame response to the plasma, as well as flame regulation for direct coupling between the discharge and the flame. Plasma, when it is applied to hydrocarbon flames, generates ionic wind due to the electric body force on the charge carrying species. The ionic wind has been shown to influence flame behavior, propagation speed, and stability of flames. In recent years, flame behaviors in PAC also obtained some attention. The deformation of co-flow diffusion flame with the plasma was experimentally investigated [26]. When the plasma was generated between the electrodes, the flames were strongly distorted and regularly extended toward the one electrode. A similar phenomenon could be also observed in a hydrogen diffusion flame combined with a plasma actuator [27]. But, the flames extended in the opposite direction under the influence of plasma compared to the study in Ref. [26]. Tang et al. [28] discussed the manner which the coaxial dielectric barrier discharge (DBD) plasma served as a disturbance to the laminar premixed flame. Results showed that the disturbance can either deflect the flame sheet or oscillate the flame edge. They correlate the fluctuation and deflection of the flame with the instability of the heat release rate. Despite many efforts in plasma-assisted combustion research, quantitative or even qualitative understanding of the flame behavior with plasma coupling has not been well-accomplished.

Plasma provides an unprecedented opportunity for combustion and emission control owing to its unique capability in producing active species and heat and modifying transport processes. Plasma-assisted combustion was developing intensively, while the related technique in flame characteristic diagnosis by optical method were very scarce. The effective and good diagnostics method on the plasma-assisted combustion can be beneficial for better utilization of energy and reduce the pollutants formation. Based on the basic idea of flame quantification in the fire field, this study conducts to define and analyze the flame characteristics in the direct coupling between the small-scale plasma and the flame. On the other hand, to the best of our knowledge, few studies reported the detailed influences of the direct plasma coupling on soot emission and temperature distributions. The major difficulty lies in the interference of the simultaneous luminescence of plasma and flame on the flame diagnosis. In our study, it could provide an optical diagnostic method combined with effective separation of the flame intensity from the plasma one and obtain the two-dimensional soot emission and temperature distribution in flames.

In this paper, the optical diagnostic method including extraction of flame morphologic characteristics, and the two-dimensional distributions of the temperature and the *KL* factor were described in Section 2. Some results and discussion about the effects of electrical parameters associated with plasma on the flame behavior and soot emission were given in Section 3. After that, some conclusions were outlined in Section 4.

2. Experimental methodologies

2.1 Experimental setup

Fig. 1 depicted the schematic of the experimental system, which was composed of a combustion system, the double DBD electrode assembly, a mixture supply system, and the data acquisition system.

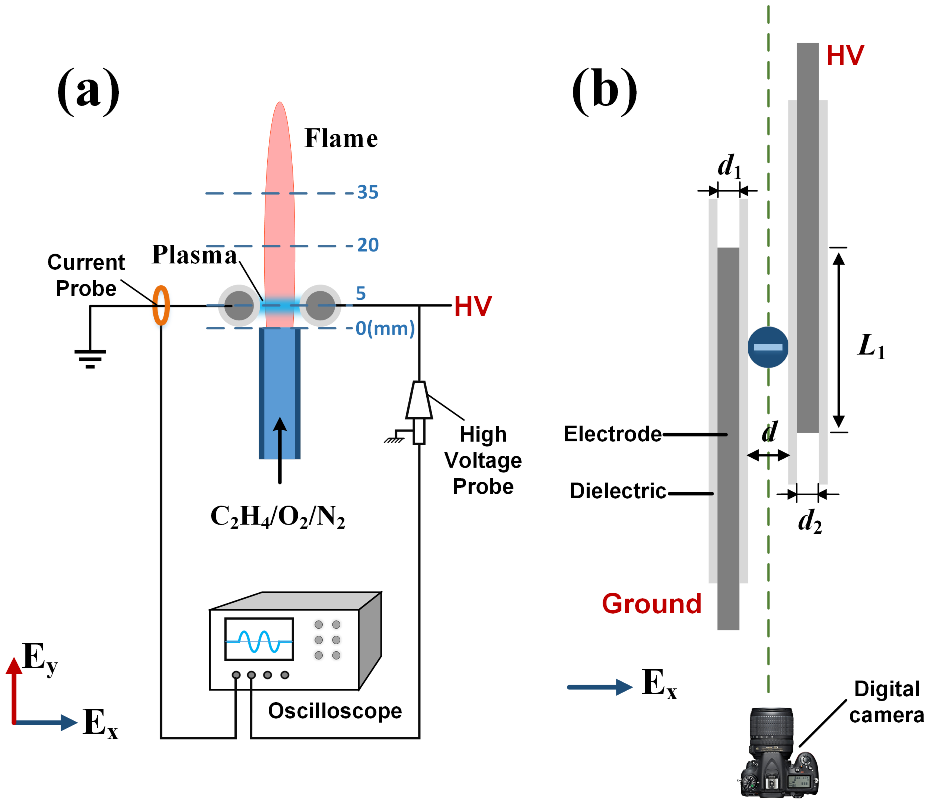

Fig. 1 Schematic diagram of experimental set up: (a) front view, (b) vertical view. Burner outlet dimensions 0.4 mm × 4 mm, diameter of stainless steel electrode rods d_1 = 4 mm, electrode overlap L_1 = 40 mm, the outside diameter of alumina ceramic tubes d_2 = 6 mm, electrode gap d = 5 mm. The electrode plane is located at different heights above the burner outlet.

In the present study, ethylene was selected as the base fuel because ethylene had been widely and extensively used for soot fundamental studies [31-33]. For the present experimental study, an ethylene partial premixed flame was formed at the burner outlet.

This flame form was chosen for two main reasons: (1) to avoid the deposition of soot on the insulating medium, (2) to avoid changing the soot distribution due to the contact of the flame with the electrodes. The burner made of quartz had a rectangular exit slot of 0.4 mm (L) × 4 mm (W) and a length of 150 mm to ensure a fully developed laminar flow profile. The flow rates of ethylene, oxygen, argon, and nitrogen were controlled by mass flow controllers (MFC) with 98% accuracy. The combustor provided ample access for the discharge electrodes applying the electric field across the flame radially at a certain height above the burner outlet. The simple structure and flexibility at multiple pressures made the DBD a good alternative to manipulating combustion for plasma actuators. The electrodes were located at different heights symmetrically above the burner exit, including 5 mm, 20 mm, and 35 mm (noted as H05, H20, and H35), as shown in Fig. 1(a). The discharge was generated between two parallel cylinder stainless steel electrodes with $d_1 = 4$ mm in diameter, covered by alumina ceramic tubes with the outside diameter of $d_2 = 6$ mm. The length of the electrode overlap was $L_1 = 40$ mm. Two parallel insulating rod electrodes were used to prevent the discharge fila-mentation and generate a more diffuse plasma. The discharge gap ($d = 5$ mm) between two electrodes was set directly above the nozzle along the axis of the premixed flow. The electrodes were powered by a custom-made high-voltage pulse generator with a peak-to-peak voltage of 20 kV and a frequency of 50 kHz. The applied voltage and current waveforms were measured by a high voltage probe (the Tektronix P6015A, bandwidth 75 MHz) and a current probe (Pearson 6585), respectively. All the electrical signals were sampled by a four-channel digital oscilloscope (TDS2024C). The sample rate of the oscilloscope is 2 GS/s. Two distinct current pulses are clearly visible. The first pulse occurs at the rising front of the voltage pulse and the second current pulse occurs at the falling front of the voltage. Fig. 2(a) plotted the typical applied voltage (*U*) and the total current waveforms for a gap distance of 5 mm. Fig. 2(b) showed the image of the plasma discharge from the top view. To shield the flame from dust or ventilation from the surroundings, the transparent box made of polymethyl methacrylate was applied, which was evenly set up with gas inlets around the box and outlets on the top of the box. The combustion system and the discharge system were housed in this box.

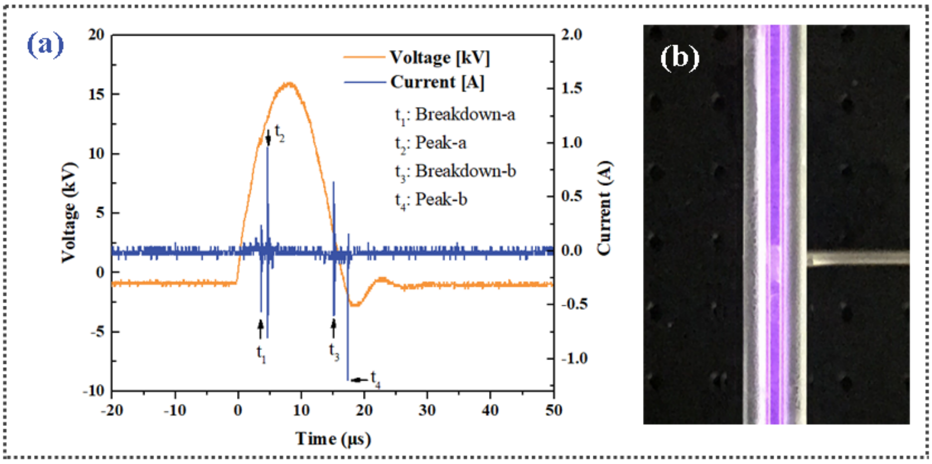

Fig. 2 (a) Applied voltage, current waveforms and (b) image of discharge sustained.

2.2 Measurements of flame behaviors

A digital single-lens reflex camera (1920 × 1080 pixels, 50 fps) was employed to record the flame morphologic characteristics from the front-view. The position of the digital camera was fixed in the experiments, as shown in Fig. 1(b). The above methods needed to be validated due to the errors caused by the difference in camera angle of views before experiments (shown in supplementary C). The image could be divided into the flame region and the non-flame region. The distinction between the two regions was determined by the brightness value of the image pixels. The image processing method was similar to the method developed by Hu et al. [35, 36]. The flow chart of the image processing procedure was shown in Fig. 3(a)-(d). The extracted continuous flame images (Fig. 3(a)) were converted into grayscale images (Fig. 3(b)) to determine the brightness of each point on the images. Based on the grayscale pixel values and threshold values, the grayscale images were converted into binary images (Fig. 3(c)). The point whose luminance was higher than the threshold value was considered the flame, and the point whose luminance was lower than the threshold value was the non-flame.

$$\text{if } I(x, y) \geqslant \text{level}, I(x, y) = 255 \tag{1}$$

$$\text{else if } I(x, y) < \text{level}, I(x, y) = 0 \tag{2}$$

The "level" value in the equations is not a fixed value. The formula here is for readers to understand the distinction between flame area and non-flame area in the binary image in this method. The consecutive binary images were averaged to achieve the average images (Fig. 3(d)). Fig. 3(e) shows a typical flame intermittency contours with plasma coupling. The intermittency (I) is defined as the fraction of the time, which represents the probability of the flame appearing at the z height [37]. It gradually decreases from a constant value of 1 to 0 as the height increases. The flame intermittency contour is obtained by analyzing the recorded consecutive flame images (1500 frames, 30 s) as applied in [33], where the mean flame morphologic parameters are determined at intermittency of 50% (i.e., $I = 0.5$). The relative uncertainty of flame morphologic parameter measurements was less than 8.0% with 95% confidence. Each condition was repeated three times.

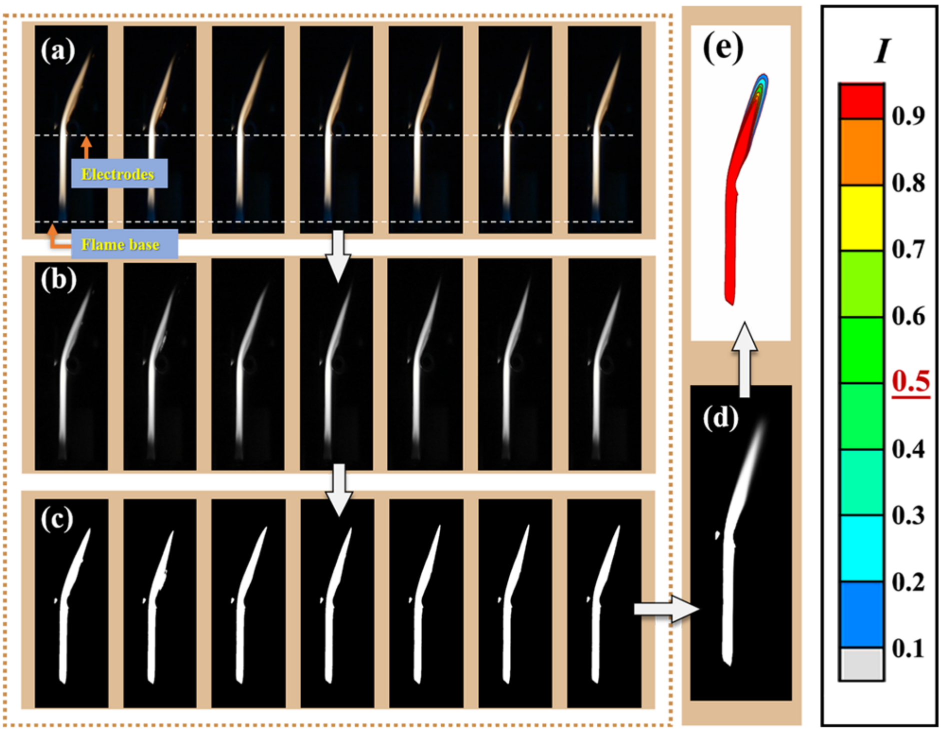

Fig. 3 Typical image processing of the flame and mean flame morphologic parameters at intermittency of 50%. ((a): original image, (b): gray image, (c): binary image, (d): average image, (e): the intermittency contour image.)

Fig. 4 showed typical flame intermittency contours. In this study, the flame morphologic parameters included three types, i.e., the flame height, horizontal extension distance of the flame, and the deflection angle. The flame height from the burner outlet to the bottom of electrodes (labeled $Z_{f,T}$), which was a constant value, was independent of the plasma coupling. The flame height above the electrodes ($Z_{f,0}$: without plasma, $Z_{f,p}$: with plasma), the flame horizontal extension distance ($L_{f,0}$: without plasma, $L_{f,p}$: with plasma), and the deflection angle (θ_0: without plasma, θ: with plasma) were subject to the plasma and other factors. The above parameters were defined from the contour at intermittency $I = 0.5$. Each test condition was repeated three times.

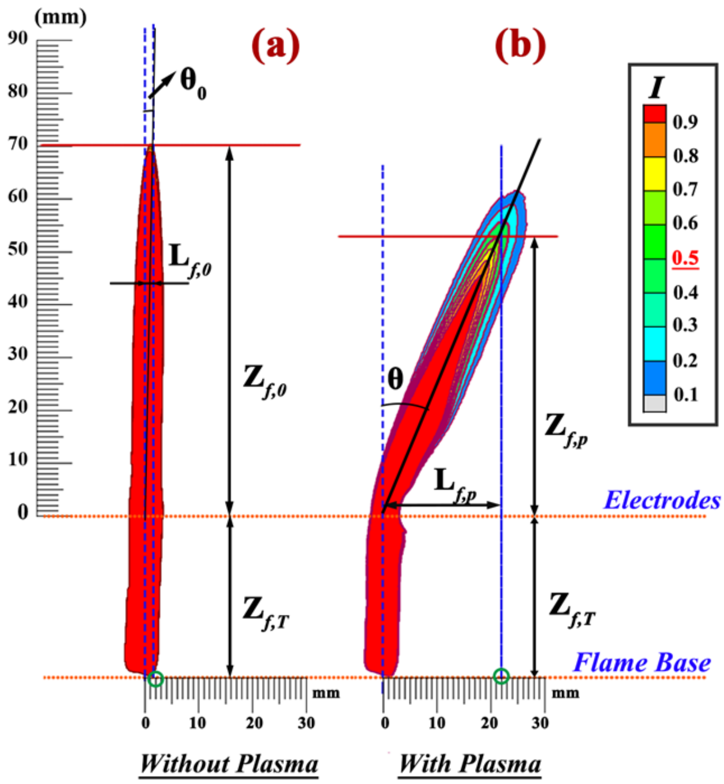

Fig. 4 Typical flame intermittency contours and definition of flame characteristic parameters ((a) without plasma coupling, (b) with plasma coupling).

2.3 Novel extraction method for two-dimensional temperature and *KL* factor distributions

Since it was rough and difficult to measure flame temperatures using thermocouples due to the existence of an electric field in the flame, optical diagnostic like the two-color method was selected to measure the two-dimensional distribution of temperature and the *KL* factor. This method had been widely used in the nonintrusive in-situ diagnostics of combustion behavior [38-42], and it was approved that this method is effective for flame and soot diagnostics. However, the two-color method could not be directly applied to the flame coupled with plasma, because the intensity emitted by plasma disturbed and overlapped the intensity from the flame. In this paper, a novel method could eliminate the luminescence of plasma in the field of view via changing imaging parameters (Photosensitivity) without affecting the flame structure. Fig. 5 showed the image processing procedure of plasma filtration under the plasma-flame coupling. Fig. 5(a) illustrated the front view of two parallel electrodes. The position of the flame relative to the electrodes was shown in Fig. 5(b). When the plasma was generated, flame and plasma emitted light simultaneously and there were overlapping regions delineated by the purple ellipse in Fig. 5(c). In this paper, the plasma luminescence area was small enough, and the spectrum of the plasma and flame luminescence in the overlapping region are different. There was an assumption that the intensity of plasma emission in the absence of flame was the same as that in the plasma coupled with flame. Therefore, we filtered out the plasma luminescence without flame by adjusting the imaging parameters. Then, the imaging parameters satisfying the above conditions are applied to the flame with the plasma coupling, as shown in Fig. 5(d).

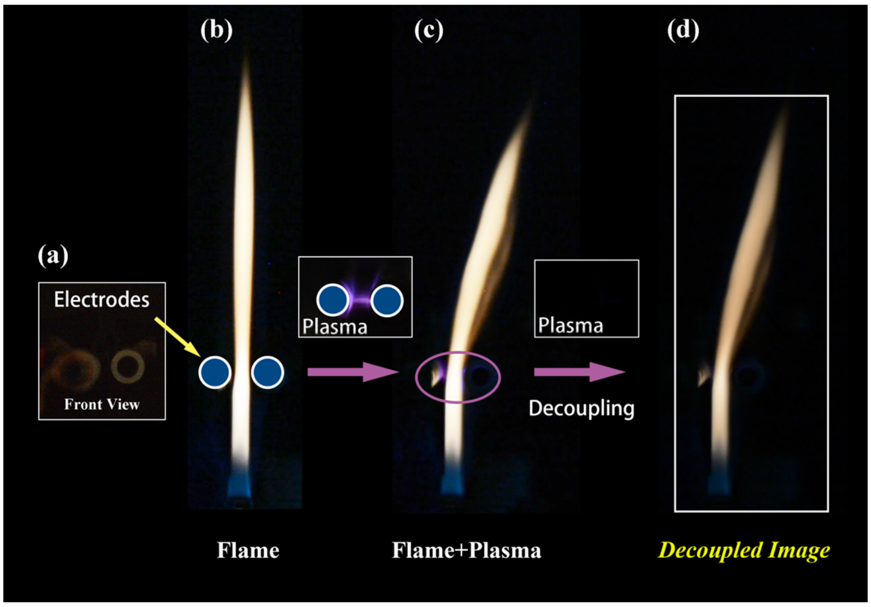

Fig. 5 The decoupling process of plasma-flame luminescence and flame extraction. (a) The relative position of the electrodes under the front view. (b) The position of the flame relative to the electrodes without plasma. Plasma-flame luminescent simultaneously (c) before and (d) after decoupling.

For plasma removal in the field of view, by keeping other parameters of the camera unchanged and only changing the photosensitivity, the plasma imaging under different camera parameters was obtained. The RGB values of images were acquired by image processing. To reduce the effect of noise, the 26×21 pixels from the same location of sixty images were selected to obtain the average RGB value of plasma luminescence, as shown in Fig. 6(d). The plasma-background overlapping radiation (labeled P) images' RGB values were obtained shown in Fig. 6(a) correspondingly for different photosensitivity from 100 to 3500. Fig. 6(b) showed the variation of the RGB value of the background (labeled B) at the same position for different photosensitivity. Fig. 6(c) plotted the difference of the RGB values (labeled $(P\text{-}B)_{R,\,G,\,B}$) between the plasma-background overlapping luminescence and the background luminescence without plasma at different photosensitivity, which represented the RGB value of plasma luminescence. As the photosensitivity decreased, the value of $(P\text{-}B)_{R,\,G,\,B}$ decreased respectively. In this study, a small value sufficiently was set to 0.5, denoted as ε. When the maximum value of the $(P\text{-}B)_{R,\,G,\,B}$ at certain photosensitivity was less than or equal to ε, it was considered that the plasma luminescence in the field-of-views could be ignored. Although this method provided the possible feasibility of the method above, digital imaging was affected by numerous factors, such as the external environment, the flame luminescence spectral response, and the intensity emitted by the plasma.

Therefore, the imaging parameters should be adjusted appropriately for different shooting subjects.

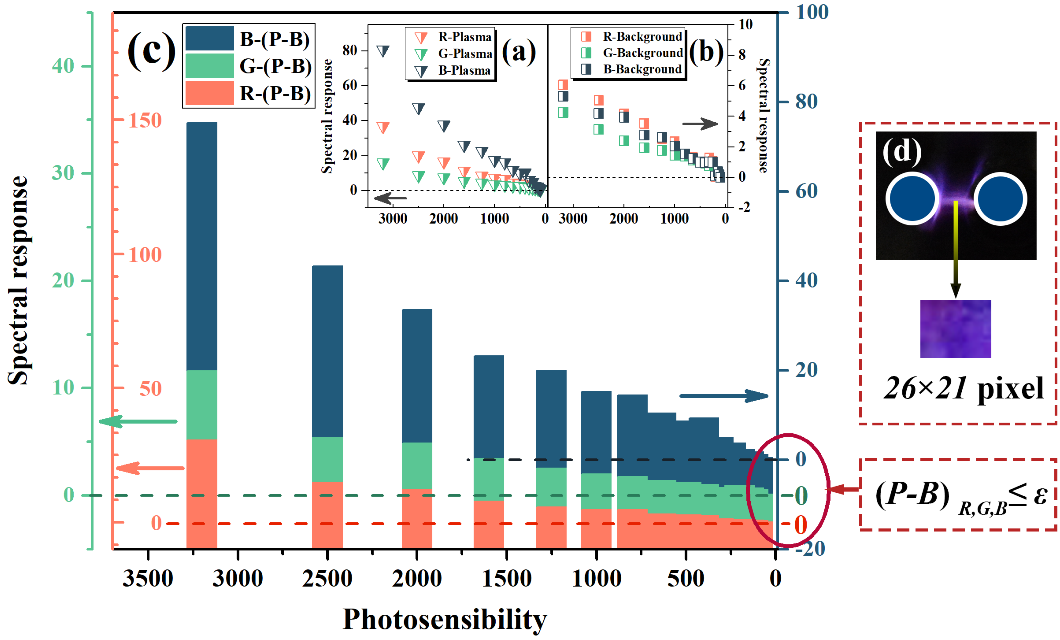

Fig. 6 The RGB values as the photosensitivity changes, (a) Plasma-Background overlapping luminescence (labeled *P*), (b)Background luminescence (labeled *B*) and (c) Plasma luminescence $(P\text{-}B)_{R,\ G,\ B}$. (d) Calculation area.

The detailed principle and derivation process of the two-color method were shown in_Supplementary Materials Parts A and B. It had been proven that the *KL* factor was proportional to the soot emissions in the flame [44]. Based on the empirical correlation [30, 43], the soot emissions could be qualitatively by the *KL* factor. The exposure time and aperture value of the camera were set as 1/500 s and f-9, respectively. The focal length was set to be 85 mm. Red (700 nm) and green (546 nm) wavelengths were selected as the measurement temperature bands. It should be noted that the temperature distribution measured by this method represented the soot particle temperature. The temperature of the combustion gases cannot be directly measured. However, these temperatures were still useful to illustrate the temperature levels and compare different combustion processes for different discharge and flame conditions based on the same standard. For the unsteady flame with plasma coupling, the distribution of two-dimensional temperature and *KL* factor was calculated five times under the same operating conditions. The average values were used for further analysis.

3. Discussion

3.1 Flame instability analysis

The oscillation of a premixed flame was attributed to the direct coupling of the plasma on the flame. The supplementary movie showed a typical oscillating flame deforming into the shape as shown in Fig. 3(a) with plasma coupling. To study the effects of plasma-flame coupling on flame behavior, it was necessary to quantify the oscillating flame. As the definition in section 2.2, each condition was repeated three times. The experimental uncertainty could be estimated with

$$X_i = X_i(\text{measured}) \pm \delta X_i \quad (3)$$

$$\sigma = \sqrt{\frac{\sum_{i=1}^{n} (X_i - \overline{X})^2}{N-1}} \quad (4)$$

where the value of X_i (measured) represented the mean value of a set of N observations in a multiple-sample experiment. The value of δX_i represented 2σ for sample analysis (i.e., $\delta X_i = 2\sigma$), where σ was the standard deviation of the population of measurements. Since 95% of all the elements were within $\pm 2\sigma$ of the average value [54,55], we could estimate that the mean value must be within $\pm 2\sigma$ of the observation with 95% confidence. The average values are used for further analysis. Fig. 7 showed the typical flame intermittency contour of three repeats as an example. The relative uncertainty ($2\sigma/Average$) of the flame morphologic parameter measurements for all the tests were found to be less than 8.0% with 95% confidence (i.e., $2\sigma/Average \leq 8.0\%$). The typical data is demonstrated in Table 1, which showed the variation of characteristic parameters under the impact of discharge frequency. More detailed data could be found in Table S1-S5. The oscillation in flames was also found in previous studies [45]. This effect was most likely caused by the residual electric field after the discharge pulse, producing the electrohydrodynamic force ("ion wind") on the charges generated during the discharge.

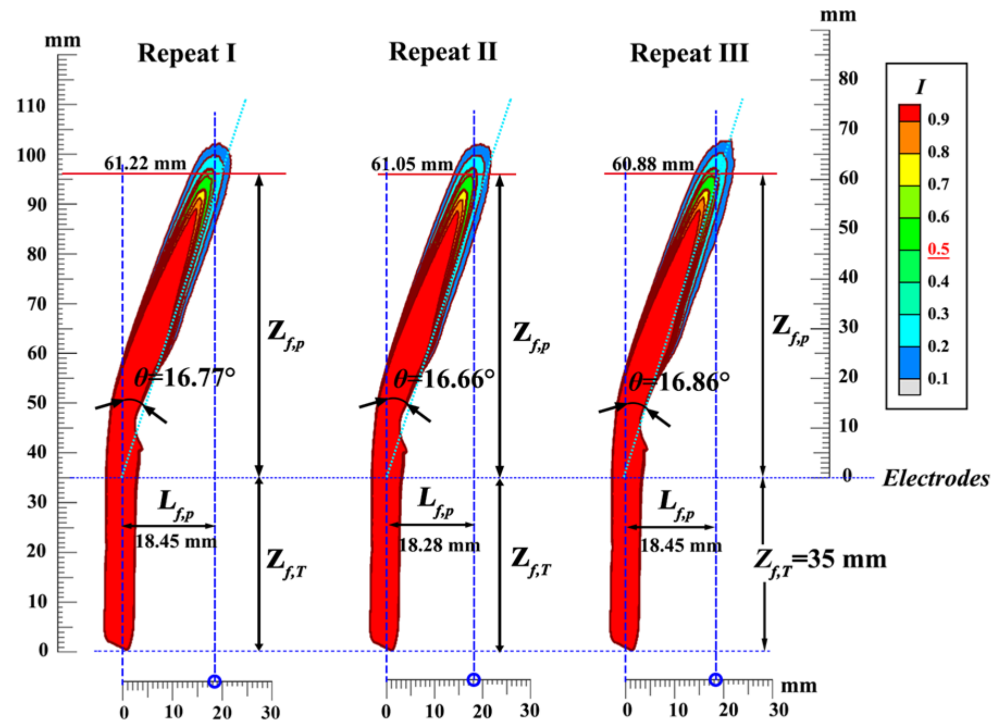

Fig. 7 Typical flame intermittency contour for three repeats.

Table 1. Estimation of the measurement uncertainty of the typical flame morphologic parameters ($Z_{f,\,p}$, $L_{f,\,p}$, θ) at different discharge frequencies. Electrodes were placed 35 mm in height above the burner outlet.

Electrode height	*Parameter*	*f* *(kHz)*	Repeat I	Repeat II	Repeat III	*Average*	*σ*	$\frac{2\sigma}{Average}\times100\%$
35 mm	$Z_{f,\,p}$ *(mm)*	**0.5**	85.36	85.19	85.53	85.36	0.17	0.40
		1.0	83.32	82.47	81.79	82.53	0.77	1.86
		1.5	78.90	79.41	79.41	79.24	0.29	0.74
		2.0	72.27	72.44	72.61	72.44	0.17	0.47
		2.5	69.72	69.89	69.72	69.78	0.10	0.28
		3.0	67.85	67.85	67.68	67.79	0.10	0.29
		3.5	64.28	64.45	63.94	64.22	0.26	0.81
		4.0	61.22	61.05	60.88	61.05	0.17	0.56
		4.5	62.58	62.41	62.07	62.35	0.26	0.83
	$L_{f,\,p}$	**0.5**	10.20	10.03	10.03	10.09	0.10	1.95

(mm)	**1.0**	12.75	13.18	12.84	12.92	0.22	3.48
	1.5	16.75	17.26	16.58	16.86	0.35	4.20
	2.0	14.54	14.79	14.54	14.62	0.15	2.01
	2.5	15.90	15.73	16.24	15.95	0.26	3.26
	3.0	18.11	17.60	18.28	17.99	0.35	3.93
	3.5	18.11	17.94	17.94	17.99	0.10	1.09
	4.0	18.45	18.28	18.45	18.39	0.10	1.07
	4.5	22.27	21.76	22.27	22.10	0.29	2.66
	7	6.81	6.71	6.69	6.74	0.07	1.97
	8	8.70	9.08	8.92	8.90	0.19	4.25
	9	11.98	12.26	11.79	12.01	0.24	3.93
	10	11.37	11.54	11.32	11.41	0.11	2.01
***θ*(°)**	**11**	12.84	12.68	13.11	12.88	0.22	3.36
	12	14.94	14.54	15.11	14.86	0.29	3.96
	13	15.73	15.55	15.67	15.65	0.09	1.17
	14	16.77	16.66	16.86	16.76	0.10	1.14
	15	19.59	19.22	19.74	19.52	0.27	2.72

3.2 Effects of Electrical Parameters on Flame Behavior

Fig. 8 showed the typical flame shapes and intermittency contours (I) for the coupling of various plasma with different applied voltages (U). The flame height could be divided into two parts: (1) the flame height from the burner outlet to the bottom of electrodes ($Z_{f,T}$), which was a constant, insusceptible by plasma, (2) the flame height above the bottom of electrodes ($Z_{f,0}$: without plasma, $Z_{f,p}$: with plasma), which was at the mercy of the plasma. The entire flame height above the burner outlet was marked as $Z_{f,p} + Z_{f,T}$ (with plasma) or $Z_{f,0} + Z_{f,T}$ (without plasma). The flame horizontal extension distance ($L_{f,p}$, $L_{f,0}$) and the deflection angle (θ, θ_0) with and without plasma were defined by the contour at intermittency I = 0.5 (average flame appearance probability) [46,47].

3.2.1 Flame height

The photographs of the ethylene premixed flame without and with the plasma coupling were shown in Figs. 8 and 9. It could be found that the partial flame above the parallel electrodes deflected to the high-voltage electrode with plasma generation. With the coupling of the plasma with the flame, the local flame above the parallel electrodes rapidly converted the stable flame to one unsteadily and was unable to support a laminar combusting flow. In Fig. 8, the flame height increased roughly with the increase of applied voltage. As the discharge frequency increased, the reduction of flame height above the electrodes was shown in Fig. 9. The fluctuation of the flame decreased slightly with the increase of voltage, as demonstrated, while the fluctuation increased with the discharge frequency increasing. In the previous studies, with the plasma coupling, the flame height was changed significantly, due to the flame tilting effect and the change in gas entrainment and mixing [26, 29]. The inclination of the flame had a certain contribution to the reduction of the flame height. However, it was not clear whether the change of flame height was only affected by flame deflection.

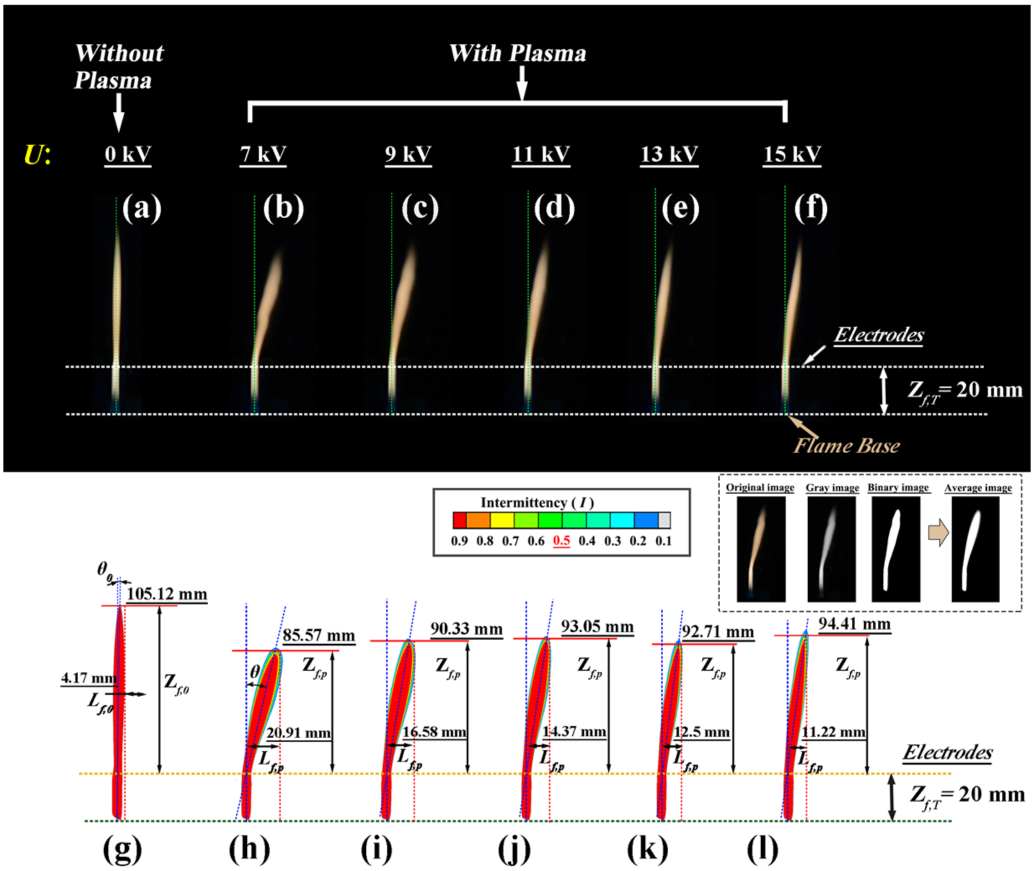

Fig. 8 Typical flames with (b)-(f) and without (a) plasma coupling of different voltages. (g)-(l) Typical flame intermittency contour. Definition of initially flame height ($Z_{f,\,0}$) and flame horizontal extension distance ($L_{f,\,0}$) without plasma, as well as the flame height ($Z_{f,\,p}$) and the flame downwind horizontal extension distance ($L_{f,\,p}$) with plasma (different applied voltages, U) on the intermittency contour. (Combustor opening: 4 mm (L) × 0.4 mm (W); f = 2.0 kHz).

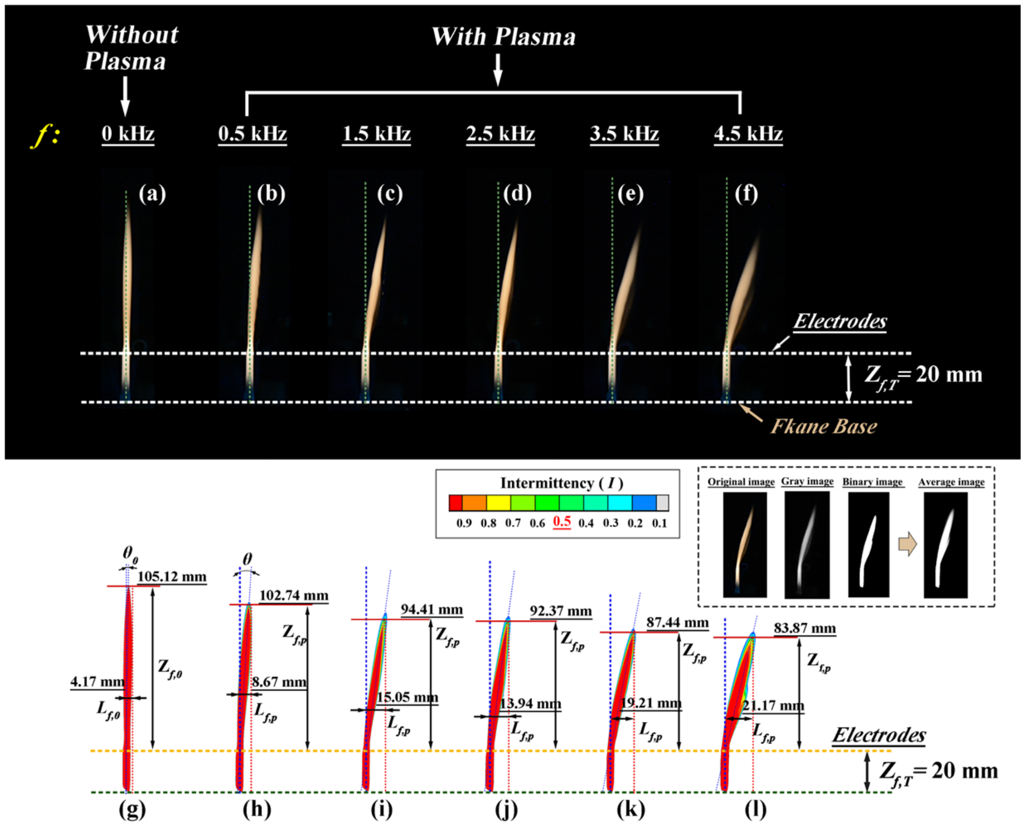

Fig. 9 Typical flames with (b)-(f) and without (a) plasma coupling of different frequencies. (g)-(l) Typical flame intermittency contour. Definition of initially flame height ($Z_{f,\,0}$) and flame horizontal extension distance ($L_{f,\,0}$) without plasma, as well as the flame height ($Z_{f,\,p}$) and the flame downwind horizontal extension distance ($L_{f,\,p}$) with plasma (different discharge frequency, f) on the intermittency contour. (Combustor opening: 4 mm (L) × 0.4 mm (W); U = 15.6 kV).

To determine the effect of flame deflection, we assumed that the partial downstream flame height affected only by flame deflection was denoted as $Z_{f,\,h}$, which was not the actual flame height above the electrode after deflection. It was assumed that the flame length above the electrode remained the same almost. The change in flame height is only affected by the deflection angle. The difference between the mean flame height without plasma ($Z_{f,\,0}$) and the measured mean flame height ($Z_{f,\,p}$) or assumed flame height ($Z_{f,\,h}$) in three discharge heights were analyzed in Fig. 10. The variation of assumed flame height above the electrodes was calculated (labeled $Z_{f,0}$ - $Z_{f,h}$) only depending on the deflection of the flame. It was found that these values fluctuate within 5 mm in Fig. 10. Nevertheless, the measured flame height ($Z_{f,0}$ - $Z_{f,p}$) decreased by at least 18 mm with the plasma generation. Therefore, the changes observable in the flame height were not only determined by the deflection of the flame, but also by the influence of the plasma itself. Sayed-Kassem et al. [56] also found that the electric field was shown to modify the flame height without deflection to promote the burning process. Therefore, the influence of plasma itself on the flame height should be considered. Besides, scholars believed that when the flame was exposed to an electric field, the visible changes in flame structure were mainly attributed to the ionic wind [48-50]. The effect of the ion wind on the flame was qualitatively similar to the results in Ref. [27] in a diffusion flame combined with a plasma, which would be discussed in detail in the subsequent sections.

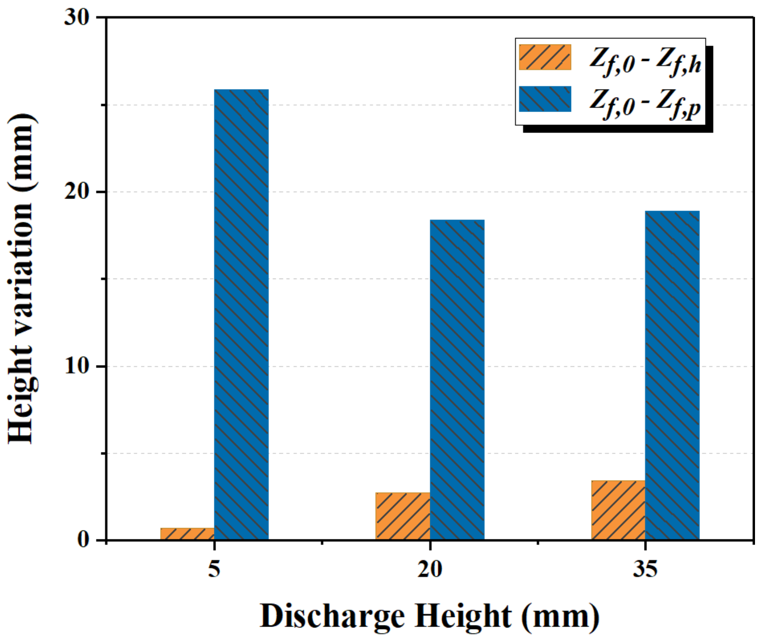

Fig. 10 Difference between mean flame height without plasma ($Z_{f,0}$) and measured

mean flame height ($Z_{f,p}$) or assumed flame height ($Z_{f,h}$) (U = 15.6 kV, f = 4.0 kHz).

In Fig. 11, measured flame heights ($Z_{f,p}$) as a function of the different electrical parameters were calculated. In Fig. 11(a), the flame height decreased with the increase of the discharge frequency at the same discharge height. A comparison of the flame height for three discharge heights was conducted with and without plasma coupling. It could be noted that the variations of flame height with discharge frequency were comparatively small for the relatively lower heights (H05 and H20). There was a more notable decrease in flame height with the higher discharge frequency for the high discharge height (H35). Correspondingly, to investigate the effect of applied voltage variation on flame behavior, different applied voltages from 7 to 17 kV were applied. The flame height presented a fluctuating within 10 mm for H05 and H20, with no obvious variation trend, illustrated in Fig. 11(b). The same fluctuation also occurred at the discharge height of 35 mm. However, the flame height under this condition presented a significant decrease with the increase of applied voltage. The reduction of flame height has also been observed by applying the high-voltage electric field [41], which was attributed to the ionic wind acting on the flow field. The flame height of a flame usually depended on the balance between axial convection and radial diffusion. The radial convection caused by the ionic wind changed the balance mechanism, which could reduce the flame height. In addition, the diminution in flame height might be referred to as an elevation in burning rate due to the electric body forces effect [56].

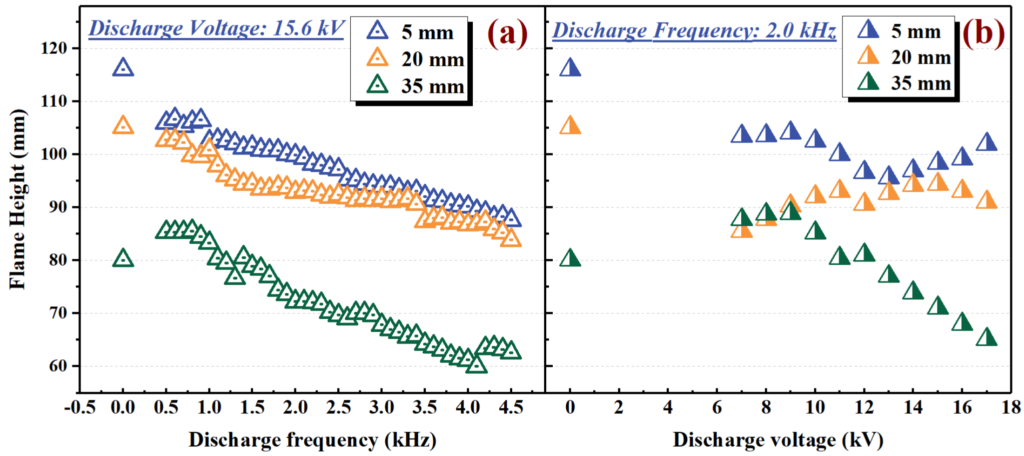

Fig. 11 The measured flame height ($Z_{f,p}$) versus the plasma with different electrical parameters, including (a) discharge frequency (f) and (b) applied voltage (U) for three discharge heights.

3.2.2 Flame horizontal extension distance and deflection angle

The flame horizontal extension distance increased with the increase of the discharge frequency, accompanied by the fluctuation instead of monotonically increasing, as shown in Fig. 12 (a). Due to the difference in plasma coupling position, the effects of different discharge heights on the horizontal flame extension distance were discrepant. At the higher discharge height (H35), it was obvious that the horizontal elongation distance of the flame increases more under the same discharge parameters. Nevertheless, the increase of applied voltage led to the decrease of flame horizontal extension distance, as shown in Fig. 12(b). Besides, the horizontal extension distance of the flame changed significantly at the relatively lower applied voltage (7-12 kV) but became little correlation with the higher discharge voltage (larger than 12 kV). With the increase of the applied voltage (7-17 kV), there was no obvious difference in the variation in horizontal extension distance in the three discharge heights.

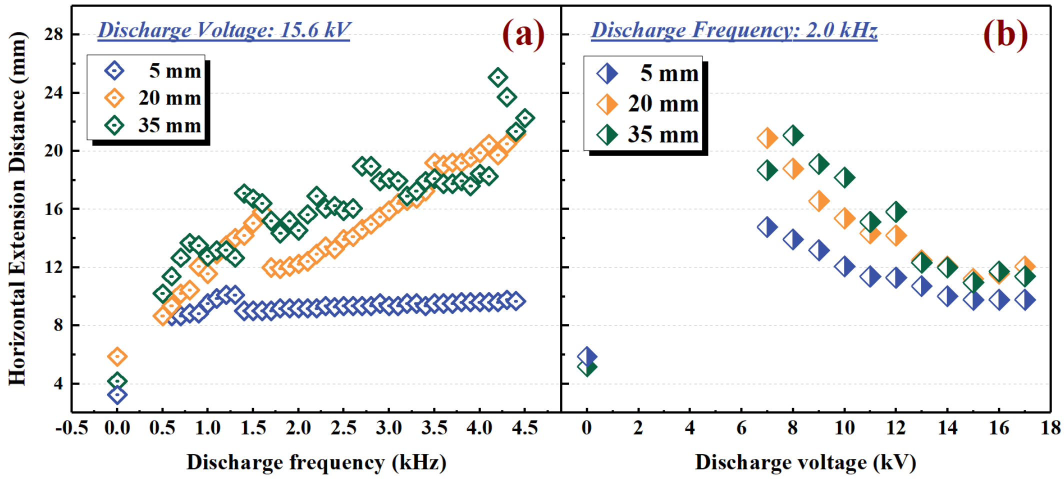

Fig. 12 The flame horizontal extension distance ($L_{f,p}$) as a function of (a) the discharge frequency (f) and (b) voltage (U) for three discharge heights.

In Fig. 13(a), the tendency of deflection angle variation was similar to the horizontal extension distance with the increase of the discharge frequency. The increase in the flame deflection angle at the same frequency range was more pronounced for the higher discharge height (H35). For the increase of applied voltage, the deflection angle decreased, as shown in Fig. 13(b). However, with the increase of applied voltage, the trend for the decrease of the deflection angle was no obvious discrepancy in the three discharge heights. In addition, the deflection angle of the flame fluctuated within the range of 5-8°.

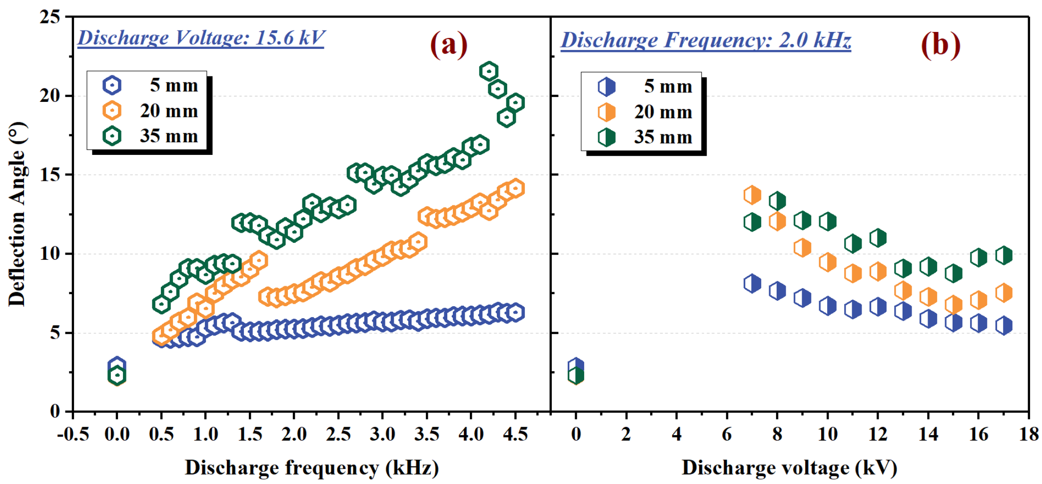

Fig. 13 The flame deflection angle (θ) as a function of (a) the discharge frequency (f) and (b) voltage (U) for three discharge heights.

3.3 Dynamics of flame behavior

The results above suggested that the variation of the flame morphologic parameters should be related to the physical mechanism of the plasma. Within the scope of the discharge parameters in this study, the three flame behavior parameters had some rules with the changes in electrical parameters.

Fig. 14 plotted the normalized total flame height ($\frac{Z_{f,p}+Z_{f,T}}{Z_{f,0}+Z_{f,T}}$) versus the discharge frequency and voltage. The piecewise relationship between the normalized total flame height and the discharge frequency could be fitted in Fig. 14(a)-(c), with different colors representing segments and dashed lines representing fitted curves. The specific values were shown in Table S6, corresponding to three discharge heights (H05, H20, and H35). The trend of dimensionless height over a set frequency range could be represented by a quadratic polynomial fitting in six segments. Besides, with the increase of the discharge frequency, three processes of normalized flame height were identified (rapid descent stage, relatively stable stage, and second descending stage). For H05, the rapid descent stage had a smaller slope and fluctuation than for H20 and H35. The normalized flame height of H05 required a higher discharge frequency to enter the relatively stable stage. It could be found that the higher the discharge heights, the greater the overall slope of the height changed. These results proved that the flame with plasma coupling at the higher discharge heights was more sensitive to the plasma effect during the increase of discharge frequency. Similar to the discharge frequency, the relationship between the normalized total flame height and the applied voltage could be fitted and expressed by a quadratic polynomial, as demonstrated in Table S7. It could be seen that the change of dimensionless flame height with applied voltage can be divided into two stages in Fig. 14(d)-(f), with 12 kV as a demarcation point.

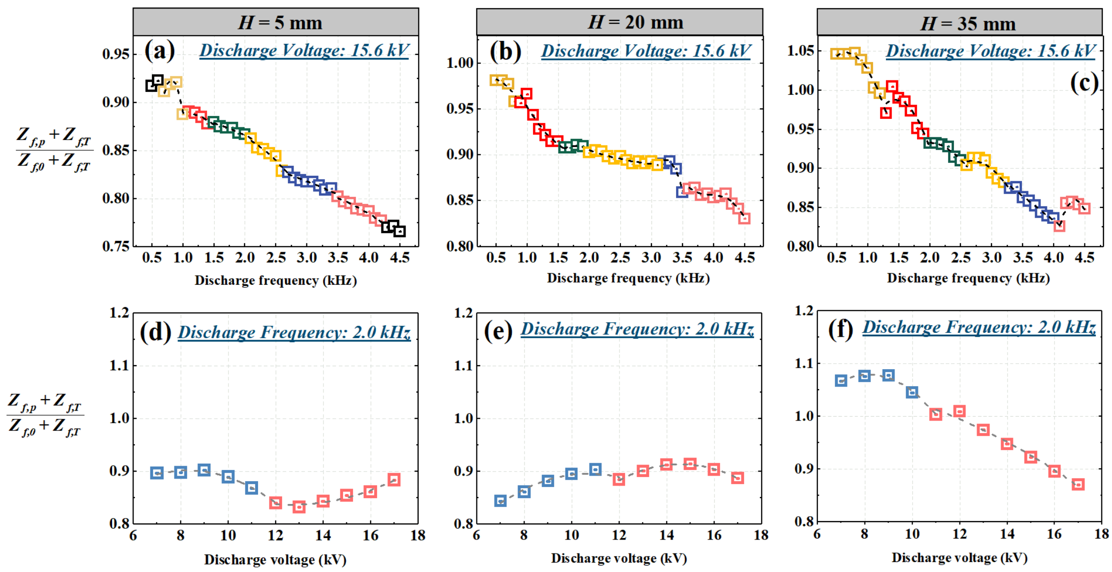

Fig. 14 Plotting of normalized total flame height $(\frac{Z_{f,\,p}+Z_{f,\,T}}{Z_{f,\,0}+Z_{f,\,T}})$ against the discharge frequency ((a)-(c)) and voltage ((d)-(f)). The piecewise relationship was represented by a different color, and the fitted curves was depicted with a black dotted line.

Based on the flame intermittency contours (I) as exemplified in Fig. 9, 2D scatter plots of the horizontal extension distance ($L_{f,\,p}$) versus the electrical parameters were depicted in Fig. 15. Within the scopes of the set frequency, the variation of horizontal extension distance escalated piecewise. In the range of 0.5-1.5 kHz, the horizontal extension distance had a rapid increasing process under the conditions of H05 and H20. In the second stage, there was initially a sharp decrease compared to the later stage (about 1.5 kHz) of the first stage. Later, with the increase of the frequency, the horizontal extension distance increased, as shown in Fig. 15(a)-(b). At the same time, the growth amplitude of H20 was greater than that of H05. Besides, as the discharge frequency increased, the horizontal extension distance showed stronger fluctuations at higher discharge heights (H35), as shown in Fig. 15(c). The function of flame horizontal extension distance and discharge frequency could be fitted to polynomial, as shown in Table S8. In Fig. 15(d)-(f), the horizontal extension distance of the flame decreased with the increment of the voltage. The flame horizontal extension distance ($L_{f,\,p}$) as a function of the applied voltage (U) could be expressed by a quadratic polynomial (Table S9). It was noted that the data of Table S9 showed relatively more scatter for H35 (Fig. 15(f)) than for lower discharge height (H05 and H20).

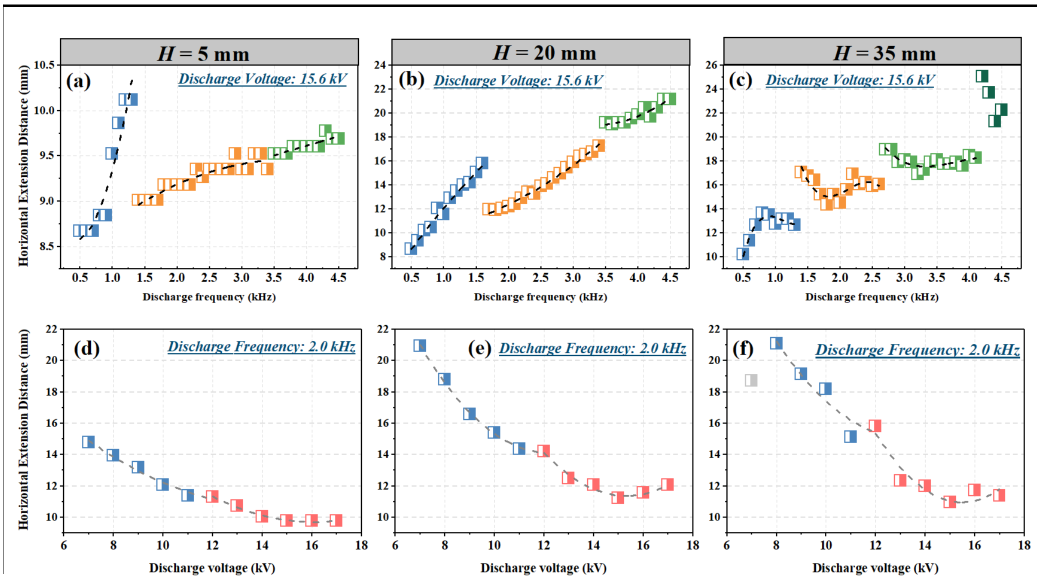

Fig. 15 Flame horizontal extension distance ($L_{f,\,p}$) as function of the discharge frequency ((a)-(c)) and voltage ((d)-(f)) for three discharge heights.

To study the amplitude of the overall deflection of the flame above the electrode, Fig. 16 illustrated the variation of the deflection angle with the discharge parameters. In the discharge frequency from 0.5 to 4.5 kHz, the flame deflection angle gave an analogical increasing tendency for three discharge heights. For instance, there was a noticeable fluctuation between 1 and 1.6 kHz, as shown in Fig. 16(a)-(c), and the degree of fluctuation increased with the rising of discharge height. The trend of the flame deflection angle over a set frequency range could be represented by a quadratic polynomial fitting in six segments. At higher discharge heights, the increase of deflection angle was greater under the same electrical parameters. The functional relationship between the deflection angle and the discharge frequency was represented by the quadratic polynomial in Table S10. Additionally, in Fig. 16(d)-(f), the deflection angle reduced overall with the increase of applied voltage. It could be seen that the change of dimensionless flame height with applied voltage could be divided into two stages in Fig. 16(d)-(f). Table S11 provided the flame deflection angle as a function of the applied voltage.

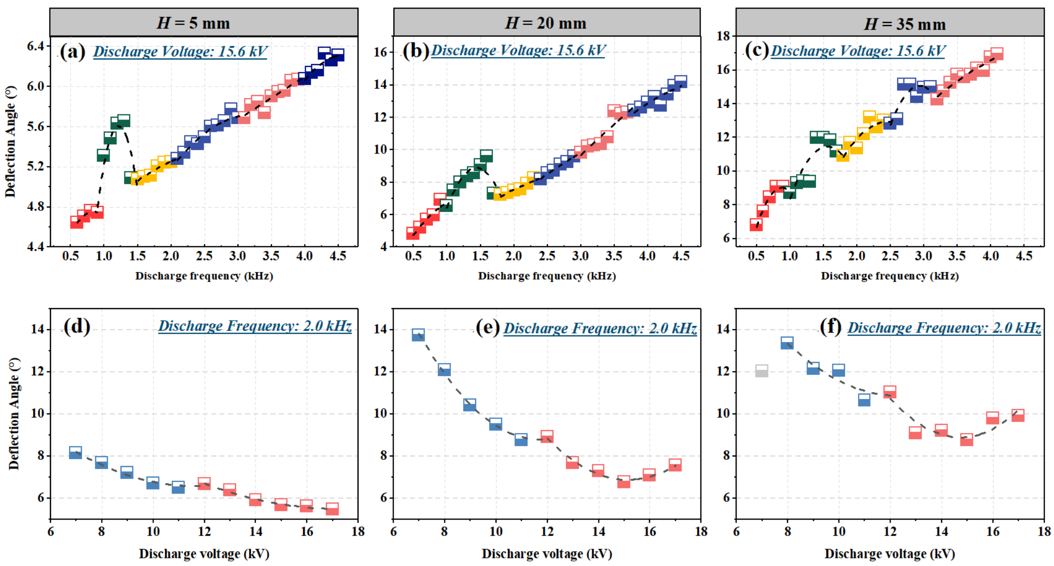

Fig. 16 Flame deflection angle (θ) as function of the discharge frequency ((a)-(c)) and voltage ((d)-(f)) for three discharge heights.

3.4 Temperature and *KL* factor distributions

The typical flame images with and without plasma coupling at different discharge heights are shown in Fig. 17. At the same discharge height, it could be observed in Fig. 17 that the luminous intensity from the radiation of soot particles decreased rapidly with the increase of discharge frequency. There might be two main reasons responsible for this phenomenon. The first one might be attributed to the ionic wind acting on the flow field as mentioned in section 3.2.1. The other factor was the reduced soot formation (which will be demonstrated indetail later), which could decrease the flame luminosity and also led to a shorter path for soot particles before it was oxidized out the flame reaction zone. However, the increase of applied voltage might lead to the opposite results for H05 and H20. As mentioned in section 3.2.1, the fluctuation of the flame decreased slightly with the increase of voltage, as demonstrated while the fluctuation increased with the discharge frequency increasing. This phenomenon applied to the plasma-flame coupling at all three heights.

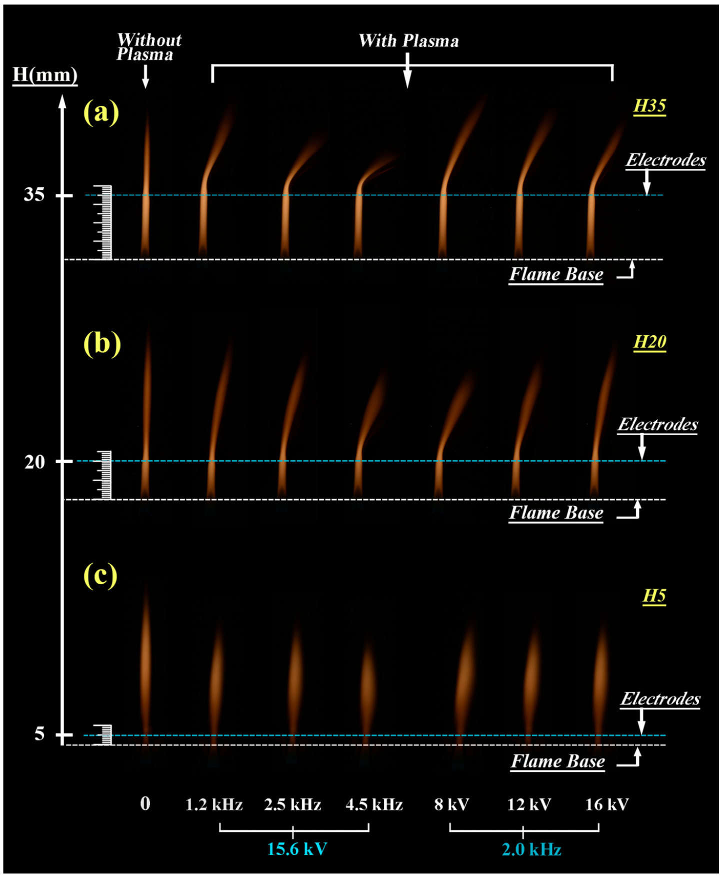

Fig. 17 Typical images of flames with and without plasma coupling at different discharge heights ((a) 35 mm, (b) 20 mm, (c) 5 mm).

The measured distributions of temperatures in three discharge heights at various electrical conditions were presented in Fig. 18. The overall partition of flame temperature was unaffected by the plasma-flame coupling. When the plasma couple with the flame, it should be paid close attention to that the temperature distribution of the flame had no significant change from the burner outlet to the electrodes compared to that without plasma. The temperature distribution of the local flame above the electrode changed under the direct plasma coupling.

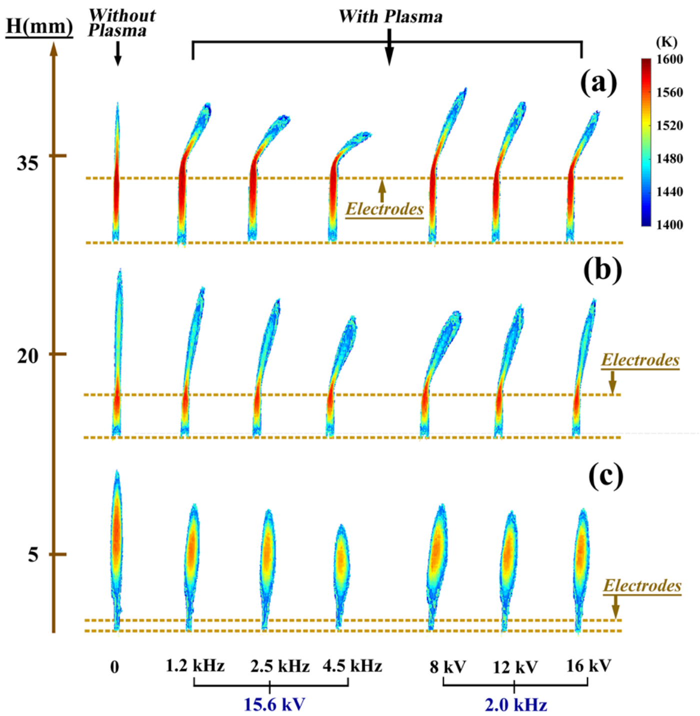

Fig. 18 Temperature distributions with various discharge conditions at different discharge heights ((a) 35 mm, (b) 20 mm, (c) 5 mm).

In Fig. 19(a)-(b), the effect of plasma coupling on the variations of maximum flame temperatures (T_{max}) was presented. In the case of no plasma coupling, the max temperature was 1564 K for H05. It was found a decrease of the maximum flame temperature (1554 K) as the plasma generation at 1.2 kHz in Fig. 19(a). Then, as the discharge frequency increased to 4.5 kHz, the results demonstrated that the maximum flame temperature decreased to 1544 K for H05. In Fig. 19(b), the max temperature of H05 decreased first from 1564 to 1553 K and then remained constant as the plasma with a higher voltage coupled to the flame. As visualized in Fig. 17(c), the position of the plasma coupling was close to the exit of the burner. The max temperature was affected by plasma coupling because the high-temperature area of the flame was located above the electrodes. At the higher discharge heights (H20, H35), the maximum flame temperature increased slightly with the plasma addition. With the increase of applied voltage and frequency, the max temperature had no significant change for the condition of H20 and H35. This might be attributed to the high-temperature zone of the flame located at or below the location where the plasma is generated, as shown in Fig. 18(b)-(c). The local flame from the burner outlet to the electrodes was independent of the plasma coupling.

Since the partial flame from the burner outlet to the electrodes was independent of the plasma coupling, the average temperature of the flame was calculated by taking only the part of the flame above the electrode for different conditions of plasma coupling. First, the average temperature of the flame would decrease when the plasma generated in Fig. 19(c)-(d), which is most effective for H35. Then, as the discharge frequency increased, plasma coupling caused a decrease in the mean temperature in Fig. 19(c). With the increase of voltage, the average flame temperature rose slightly for H05 and H20. The changing trend of the mean flame temperature was consistent with those of the flame length and fluctuation in Fig. 17(a)-(b). However, with the increase of applied voltage, the flame temperature decreased first and then increased for H35.

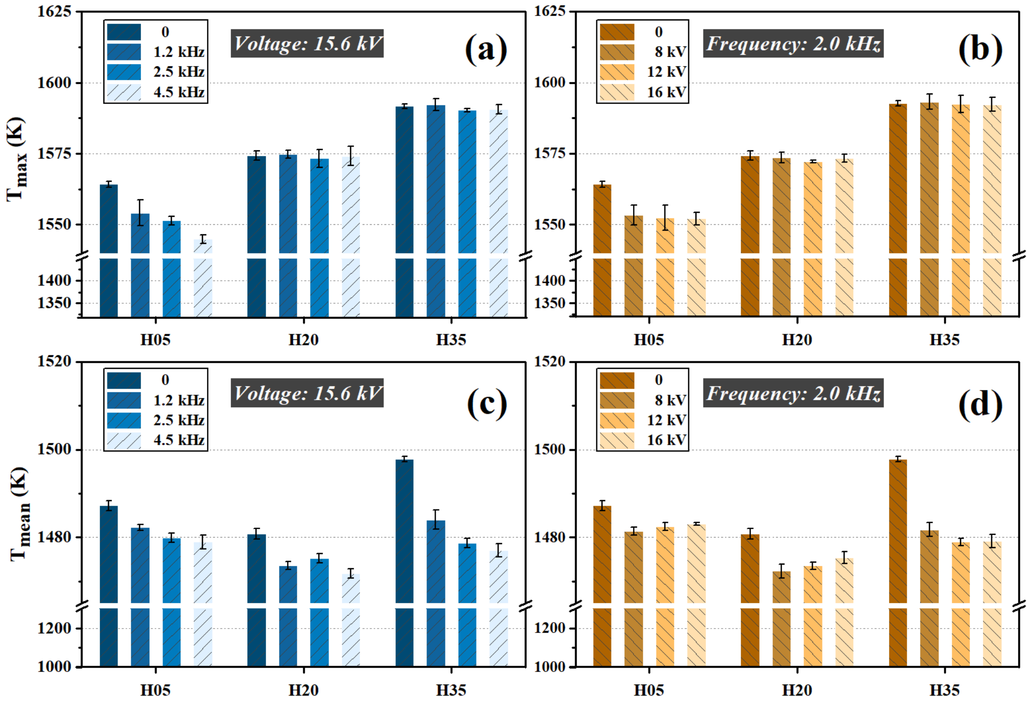

Fig. 19 The (a)-(b) maximum temperature (T_{max}) for the entire flame and (c)-(d) average flame temperature (T_{mean}) above the electrodes at different discharge heights under the action of different plasma.

The *KL* factor could be used to qualitatively compare the volume fraction of soot, the larger value of which could manifest more soot production in that region [51-54]. The synergistic effect of plasma-flame coupling on the soot emission could be experimentally examined by the two-color method at different electrical conditions. Three major factors might be responsible for the difference in the *KL* factor, including (1) the flame behavior, which might affect the residence time of soot particles in flames; (2) the flame temperature, which might affect the soot inception and surface growth rates (3) a direct effect of electric field via activation of species due to collisions with electrons and ions [55]. As illustrated in Fig. 20 (a)-(c), the distributions of *KL* factors in H35, H20, and H05 at various electrical parameters were presented, respectively.

Similarly, in Fig. 20(a)-(c), the soot emission had no significant change from the burner outlet to the electrodes compared to that without plasma, when the plasma was coupled with the flame. For the local flame above the electrode, the soot emission decreased significantly under the direct coupling of the plasma with the flame.

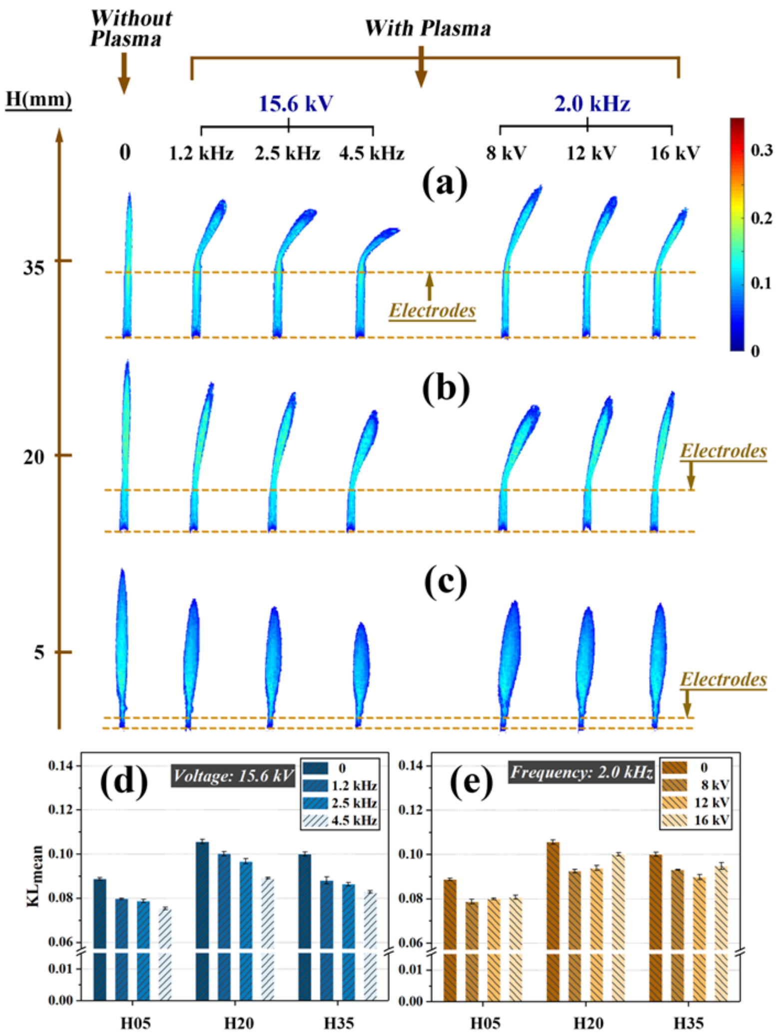

Fig. 20 *KL* factor distributions with various plasma coupling (a):H35, (b):H20, (c):H05). The average *KL* factor (KL_{mean}) as a function of (d) the discharge frequency and (e) voltages at different discharge heights.

Fig. 20(d) showed the variation trend of mean *KL* factors with the increase of discharge frequency. The effect of electric field addition in a hydrocarbon flame on soot precursor reduction was confirmed [55]. They found that the specific chemical reaction was intensified through the electron injection. In Fig. 20(d), the soot emission decreased further with the increase of discharge frequency. This effect was stronger for H35 compared to the coupling of plasma and flame at the other two altitudes (H05 and H20). The reasons for the reduction of soot in the present experiment could be explained as follows. Firstly, as the discharge frequency increased, the number of discharge channels generated per unit time appreciably increased. The number of high-energy electrons increased, and the motion of which intensified per unit of time. The collision probability of high-energy electrons and particles in the flame increased accordingly, which might promote the reduction of soot. Matsuzawa et al [55] suggested that the plasma-induced reaction intensification might contribute to convert ionic species into neutral non-soot-precursors and reduce the emission of soot precursors. Secondly, with the plasma coupling, the flame length was significantly reduced, which led to a shortened residence time for soot particle growth. This effect further conduced the reduction of the soot emission. Finally, as shown in Fig. 19(c), as the frequency increased, the decrease in flame temperature could inhibit the generation of soot. When the plasma was coupling to the flame directly, the synergy of the above three factors reduced the the amount of soot as the discharge frequency increased.

The effect of applied voltage on soot emission was exhibited in Fig. 20(e). With the increase of applied voltage (8-16 kV), the mean *KL* factor for H05 and H20 increased monotonically. However, the mean *KL* factor for H35 decreased first and then increased with the increase of applied voltage. The reasons for the variation of soot with plasma coupling could be explained as follows. Firstly, with the increase of applied voltage, the flame height gradually increased slightly for the discharge height of 5 and 20 mm, as shown in Fig. 20(b)-(c). The increase of the residence time of soot was accompanied by the increase of soot. At the discharge height of 35 mm, the soot emission at applied voltage of 12 kV was less than that at the applied voltage of 8 kV, which corresponds to the reduction in flame height in Fig. 20(a). The alteration of flame length will affect the residence time of soot growth, which further affects the soot emission. Secondly, the electric field intensity increased with the applied voltage increasing at constant discharge frequency. More gas breakdowns occurred in a single discharge cycle, which meant that the number and average energy of electrons significantly increased. More active species were produced due to the intensified reaction between electrons and gas [56], which promoted the oxidation of soot. Song et al reported the abatement capability of particulate matter (PM), hydrocarbons (HC), and NO_x as functions of voltage at the fixed frequency from an actual diesel exhaust [57]. Finally, as shown in Fig. 19(d), the variation trend of temperature was consistent with the variation of soot in Fig. 20(e). Considering the aspects above, it could be found that plasma-flame coupling at different heights had different synergistic mechanisms for soot emission as the applied voltage increased. For H05 and H20, it could be found that the influence of the electric field itself on soot generation is not the dominant factor combined with the variation of soot emission. Correspondingly, the ion wind that affecting the flame behavior and the variation of flame temperature had more obvious effects on the soot emission. Conversely, the flame height, variation of the electric field, and the temperature might be the dominant factors affecting the variation of soot emission for H35 when the voltage was less than 12 kV. When the applied voltage is greater than 12 kV, the increase of soot was mainly attributed to the increase of temperature.

4. Conclusion

In this paper, comprehensive optical diagnostics for flame behavior and soot emission under plasma-flame coupling at different heights were investigated, including quantifying the flame morphologic characteristics, and using a novel diagnostic method to decouple the plasma and flame luminescence to further extract the two-dimensional distribution of flame temperature and soot emission. The main conclusions obtained in this study were summarized as follows:

(1) For results of the flame behavior, at the same discharge height, with the increase of discharge frequency, the flame height decreased while the flame horizontal extension distance and the deflection angle increased. The flame morphometric parameters changed more remarkably with electrical parameters for the higher discharge heights. The experimental results showed the affected field of the flame behavior matched the field acted by pulse discharge, which suggested a one-to-one correspondence between plasma action and flame deflection or shortening.

(2) At the same discharge height, the flame temperature and soot decreased with the increase of discharge frequency. The soot emission changed more remarkably with the discharge frequency for relatively higher discharge heights. With the increase of voltage, the flame temperature and soot increased at the lower discharge heights (5 and 20 mm), and decreased first and then increased at the higher discharge v height (35 mm). The variation of the soot emission across the flame depended on a variety of factors, including the flame

behavior, the flame temperature, and the effect of electric field by energetic and chemically active species.

In this paper, the experimental results obtained and the optical diagnosis method proposed provided an essential basis to quantify the flame behavior from the directly coupling of the plasma with the flame. The decoupling method of plasma and flame luminescence established the foundation for optical diagnosis of flame in direct plasma-flame coupling.

CRediT authorship contribution statement

Dandan Qi: Writing - original draft, Methodology, Conceptualization, Investigation, Formal analysis. **Kaixuan Yang:** Investigation. **Xuan Zhao:** Validation, Investigation. **Danhua Mei:** Supervision, Writing - review & editing. **Yaoyao Ying:** Data curation, Project administration. **Lei Xu:** Data curation, Project administration. **Xin Tu:** Supervision, Writing - review & editing. **Dong Liu:** Supervision, Resources, Validation, Data curation, Funding acquisition, Writing - review & editing.

Acknowledgments

This work was supported by the National Natural Science Foundation of China [51822605, 52076110]; Jiangsu Provincial Natural Science Foundation of China [BK20200490]; and the Fundamental Research Funds for the Central Universities [30920031103, 30919011284].

Supplementary data

References

[1] Chu S, Majumdar A. Opportunities and challenges for a sustainable energy future. Nature 2012; 488:294-303. https://doi.org/10.1038/nature11475.

[2] Tang Q, Wang M, You X. Measurements of sooting limits in laminar premixed burner-stabilized stagnation ethylene, propane, and ethylene/toluene flames. Fuel 2019;235:178–84. https://doi.org/10.1016/j.fuel.2018.07.090.

[3] Zhen HS, Leung CW, Cheung CS. Effects of hydrogen addition on the characteristics of a biogas diffusion flame. Int J Hydrogen Energy 2013; 38:6874–81. https://doi.org/10.1016/j.ijhydene.2013.02.046.

[4] Aldhaidhawi M, Chiriac R, Bădescu V, Descombes G, Podevin P. Investigation on the mixture formation, combustion characteristics and performance of a Diesel engine fueled with Diesel, Biodiesel B20 and hydrogen addition. Int J Hydrogen Energy 2017;42:16793–807. https://doi.org/10.1016/j.ijhydene.2017.01.222.

[5] Lin B, Wu Y, Zhu Y, Song F, Bian D. Experimental investigation of gliding arc plasma fuel injector for ignition and extinction performance improvement. Appl Energy 2019;235:1017–26. https://doi.org/10.1016/j.apenergy.2018.11.026.

[6] Chen M, Liu D. Morphology and nanostructure transitions of soot with various dimethyl ether additions in nonpremixed ethylene flames at different scales. Energy and Fuels 2020;34:16705–19. https://doi.org/10.1021/acs.energyfuels.0c03305.

[7] Tamadonfar P, Gülder ÖL. Effect of burner diameter on the burning velocity of

premixed turbulent flames stabilized on Bunsen-type burners. Exp Therm Fluid Sci 2016;73:42–8. https://doi.org/10.1016/j.expthermflusci.2015.09.006.

[8] Goldsborough SS, Cheng S, Kang D, Saggese C, Wagnon SW, Pitz WJ. Effects of isoalcohol blending with gasoline on autoignition behavior in a rapid compression machine: Isopropanol and isobutanol. Proc Combust Inst 2020;000:1–10. https://doi.org/10.1016/j.proci.2020.08.027.

[9] Leonov SB, Elliott S, Carter C, Houpt A, Lax P, Ombrello T. Modes of plasma-stabilized combustion in cavity-based M = 2 configuration. Exp Therm Fluid Sci 2021;124:110355. https://doi.org/10.1016/j.expthermflusci.2021.110355.

[10] Nagaraju AS, Verma KA, Pandey KM, Das D. Numerical analysis of pl-asma combustion in scramjet engine-A review. Mater Today Proc 2021;45: 6838-51. https://doi.org/10.1016/j.matpr.2020.12.1025.

[11] Choe J, Sun W, Ombrello T, Carter C. Plasma assisted ammonia combustion : Simultaneous NO_x reduction and flame enhancement. Combust Flame 2021;228:430–2. https://doi.org/10.1016/j.combustflame.2021.02.016.

[12] Chen Y, He LM, Fei L, Deng J, Lei JP, Yu H. Experimental study of dielectric barrier discharge plasma-assisted combustion in an aero-engine combustor. Aerosp Sci Technol 2020;99:105765. https://doi.org/10.1016/j.ast.2020.105765.

[13] Feng R, Huang Y, Zhu J, Wang Z, Sun M, Wang H, et al. Ignition and combustion enhancement in a cavity-based supersonic combustor by a multi-channel gliding arc plasma. Exp Therm Fluid Sci 2021;120:110248. https://doi.org/10.1016/j.expthermflusci.2020.110248.

[14] Du CM, Yan JH, Cheron B. Decomposition of toluene in a gliding arc discharge plasma reactor. Plasma Sources Sci Technol 2007;16:791–7. htt-ps://doi.org/10.1088/0963-0252/16/4/014.

[15] Czernichowski A. Gliding arc. Applications to engineering and environm-ent control. Pure Appl Chem 1994;66:1301–10. https://doi.org/10.1351/pac199466061301.

[16] Kim HH, Takashima K, Katsura S, Mizuno A. Low-temperature NO_x reduction processes using combined systems of. J Phys D Appl Phys Relat 2001;34:604–13.

[17] Khacef A, Cormier JM, Pouvesle JM. NO_x remediation in oxygen-rich exhaust gas using atmospheric pressure non-thermal plasma generated by a pulsed nanosecond dielectric barrier discharge. J Phys D Appl Phys 2002;35:1491–8. https://doi.org/10.1088/0022-3727/35/13/307.

[18] Yu L, Tu X, Li X, Wang Y, Chi Y, Yan J. Destruction of acenaphthene, fluorene, anthracene and pyrene by a dc gliding arc plasma reactor. J Hazard Mater 2010;180:449–55. https://doi.org/10.1016/j.jhazmat.2010.04.051.

[19] Brethes-Dupouey S, Peyrous R, Held B. Removal of H2S in air by using gliding discharges. Eur Phys J Appl Phys 2000;11:43–58.

[20] Li L, Zhang Y. Study of OH radicals' spontaneous radiation of counterflow diffusion flame under non-equilibrium plasma. Proc SPIE 2019;11046. https://doi.org/10.1117/12.2522094.

[21] Cha MS, Lee SM, Kim KT, Chung SH. Soot suppression by nonthermal plasma

in coflow jet diffusion flames using a dielectric barrier discharge. Combust Flame 2005;141:438–47. https://doi.org/10.1016/j.combustflame.2005.02.002.

[22] Sun W, Uddi M, Won SH, Ombrello T, Carter C, Ju Y. Kinetic effects of non-equilibrium plasma-assisted methane oxidation on diffusion flame extinction limits. Combust Flame 2012;159:221–9. https://doi.org/10.1016/j.combustflame.2011.07.008.

[23] Gong C, Yi L, Wang K, Huang K, Liu F. Numerical modeling of plasm-a-assisted combustion effects on firing and intermediates in the combusti-on process of methanol–air mixtures. Energy 2020;192. https://doi.org/10.1016/j.energy.2019.116598.

[24] Sun W, Won SH, Ombrello T, Carter C, Ju Y. Direct ignition and S-cur-ve transition by in situ nano-second pulsed discharge in methane/oxygen/helium counterflow flame. Proc Combust Inst 2013;34:847–55. https://doi.org/10.1016/j.proci.2012.06.104.

[25] Varella RA, Sagás JC, Martins CA. Effects of plasma assisted combustion on pollutant emissions of a premixed flame of natural gas and air. Fuel 2016;184:269–76. https://doi.org/10.1016/j.fuel.2016.07.031.

[26] Simeni M, Tang Y, Hung Y, Eckert Z, Frederickson K, Adamovich I V. Electric field in Ns pulse and AC electric discharges in a hydrogen diff-usion flame. Combust Flame 2018;197:254–64. https://doi.org/10.1016/j.co-mbustflame.2018.08.004.

[27] Retter JE, Elliott GS, Kearney SP. Dielectric-barrier-discharge plasma-assisted

hydrogen diffusion flame. Part 1: Temperature, oxygen, and fuel measurements by one-dimensional fs/ps rotational CARS imaging. Combust Flame 2018;191:527–40. https://doi.org/10.1016/j.combustflame.2018.01.031.

[28] Tang Y, Yao Q, Cui W, Zhuo J, Li S. Premixed Flame Response to a Counterflowing Non-thermal Plasma Jet. Combust Sci Technol 2020;192:2280–96. https://doi.org/10.1080/00102202.2019.1640688.

[29] Park DG, Chung SH, Cha MS. Visualization of ionic wind in laminar je -t flames. Combust Flame 2017;184:246–8. https://doi.org/10.1016/j.combu s-tflame.2017.06.011.

[30] Zhou S, Su L, Shi T, Zheng T, Tong Y, Nie W, et al. Experimental stu -dy on the diffusive flame stabilization mechanism of plasma injector dri -ven by AC dielectric barrier discharge. J Phys D Appl Phys 2019;52. h -ttps://doi.org/10.1088/1361-6463/ab15cd.

[31] Alfè, M.; Apicella, B.; Barbella, R.; Rouzaud, J. N.; Tregrossi, A.;Ciajol -o, A. Structure-Property Relationship in Nanostructures of Young and M -ature Soot in Premixed Flames. Proc. Combust. Inst.2009, 32, 697−704. https://doi.org/10.1016/j.proci.2008.06.193.

[32] Ying, Y.; Liu, D. Nanostructure Evolution and Reactivity of Nascent Soot from Inverse Diffusion Flames in CO_2, N_2, and He Atmospheres. Carbon N. Y. 2018, 139, 172−180. https://doi.org/10.1016/j.carbon.2018.06.047.

[33] Yen, M.; Magi, V.; Abraham, J. Modeling the Effects of Hydrogen and Nitrogen Addition on Soot Formation in Laminar Ethylene Jet Diffusion Flames. Chem.

Eng. Sci. 2019, 196, 116−129. https://doi.org/10.1016/j.ces.2018.07.061.

[34] Otsu N. A Threshold Selection Method from Gray-Level Histograms. IEEE Trans Syst Man Cybern 1979;9:62–6.

[35] Hu L, Sun X, Zhang X, Ren F. Facade flame height and horizontal extending distance from opening of compartment fire with external sideward wind. Proc Combust Inst 2019;37:3859–67. https://doi.org/10.1016/j.proci.2018.06.201.

[36] Lu K, Wang Z, Ding Y, Wang J, Zhang J, Delichatsios MA, et al. Flame behavior from an opening at different elevations on the facade wall of a fire compartment. Proc Combust Inst 2020;000:1–9. https://doi.org/10.1016/j.proci.2020.07.094.

[37] Cetegen B M. Entrainment and flame geometry of fire plumes [D]. Pasadena, California: California Institute of Technology, 1982.

[38] Bu C, Leckner B, Chen X, Pallarès D, Liu D, Gómez-Barea A. Devolatilization of a single fuel particle in a fluidized bed under oxy-combustion conditions. Part A: Experimental results. Combust Flame 2015;162:797–808. https://doi.org/10.1016/j.combustflame.2014.08.015.

[39] Khatami R, Levendis YA, Delichatsios MA. Soot loading, temperature and size of single coal particle envelope flames in conventional- and oxy-combustion conditions (O_2/N_2 and O_2/CO_2). Combust Flame 2015;162:2508–17. https://doi.org/10.1016/j.combustflame.2015.02.020.

[40] Yuan Y, Li S, Xu Y, Yao Q. Experimental and theoretical analyses on ignition and surface temperature of dispersed coal particles in O_2/N_2 and O_2/CO_2 ambients. Fuel 2017;201:93–8. https://doi.org/10.1016/j.fuel.2016.09.079.

[41] Park DG, Chung SH, Cha MS. Bidirectional ionic wind in nonpremixed counterflow flames with DC electric fields. Combust Flame 2016;168:138–46. https://doi.org/10.1016/j.combustflame.2016.03.025.

[42] Binner E, Zhang L, Li C, Bhattacharya S. In-situ observation of the combustion of air-dried and wet Victorian brown coal. Proc Combust Inst 2011;33:1739–46. https://doi.org/10.1016/j.proci.2010.07.076.

[43] Vincent-Randonnier A, Larigaldie S, Magre P, Sabel′ Nikov V. Plasma a -ssisted combustion: Effect of a coaxial DBD on a methane diffusion fla -me. Plasma Sources Sci Technol 2007;16:149–60. https://doi.org/10.1088/ 0963-0252/16/1/020.

[44] Ren T, Zhou Y, Wang Q, Liu H, Li Z, Zhao C. Machine learning-assisted soot temperature and volume fraction fields predictions in the ethylene laminar diffusion flames. Opt Express 2021;29:1678. https://doi.org/10.1364/oe.413100.

[45] Tang Y, Simeni M, Frederickson K, Yao Q, Adamovich I V. Counterflow diffusion flame oscillations induced by ns pulse electric discharge waveforms 2019;206:239–48. https://doi.org/10.1016/j.combustflame.2019.05.002.

[46] Ju X, Gollner MJ, Wang Y, Tang W, Zhao K, Ren X, et al. Downstrea-m r adiative and convective heating from methane and propane fires with cross wind. Combust Flame 2019;204:1–12. https://doi.org/10.1016/j.com-bustfla me.2019.03.001.

[47] Gao W, Liu N, Jiao Y, Xie X, Pan Y, Li Z, et al. Flame length of buo-yan t turbulent slot flame. Proc Combust Inst 2019;37:3851–8. https://doi.org/1

0.1016/j.proci.2018.05.153.

[48] Kuhl J, Seeger T, Zigan L, Will S, Leipertz A. On the effect of ionic wind on structure and temperature of laminar premixed flames influenced by electric fields. Combust Flame 2017;176:391–9. https://doi.org/10.1016/j.combustflame.2016.10.026.

[49] Sakhrieh A, Lins G, Dinkelacker F, Hammer T, Leipertz A, Branston DW. The influence of pressure on the control of premixed turbulent flame-s using an electric field. Combust Flame 2005;143:313–22. https://doi.or-g/10.1016/j.combustflame.2005.06.009.

[50] Volkov EN, Kornilov VN, De Goey LPH. Experimental evaluation of DC electric field effect on the thermoacoustic behaviour of flat premixed flames. Proc Combust Inst 2013;34:955–62.https://doi.org/10.1016/j.proci.2012.06.175.

[51] Yi W, Liu H, Feng L, Wang Y, Cui Y, Liu W, et al. Multiple optical diagnostics on effects of fuel properties on spray flames under oxygen-enriched conditions. Fuel 2021;291:120129. https://doi.org/10.1016/j.fuel.2021.120129.

[52] Zhang J, Jing W, Roberts WL, Fang T. Soot temperature and *KL* factor for biodiesel and diesel spray combustion in a constant volume combustion chamber. Appl Energy 2013;107:52–65. https://doi.org/10.1016/j.apenergy.2013.02.023.

[53] Chen H, Su X, He J, Zhang P, Xu H, Zhou C. Investigation on combustion characteristics of cyclopentanol/diesel fuel blends in an optical engine. Renew Energy 2021;167:811–29. https://doi.org/10.1016/j.renene.2020.11.155.

[54] Jing W, Wu Z, Zhang W, Fang T. Measurements of soot temperature and *KL*

factor for spray combustion of biomass derived renewable fuels. Energy 2015;91:758–71. https://doi.org/10.1016/j.energy.2015.08.069.

[55] Matsuzawa Y, Suzuki J, Horisawa H, Kimura I. Effect of electron injection for soot suppression in hydrocarbon flames. Vacuum 2013;88:79–82. https://doi.org/10.1016/j.vacuum.2012.04.005.

[56] Sayed-Kassem A, Elorf A, Gillon P, Idir M, Sarh B, Gilard V. Numerical modelling to study the effect of DC electric field on a laminar ethylene diffusion flame. Int Commun Heat Mass Transf 2021;122:105167. https://doi.org/10.1016/j.icheatmasstransfer.2021.105167.

[57] Song CL, Bin F, Tao ZM, Li FC, Huang QF. Simultaneous removals of NO_x, HC and PM from diesel exhaust emissions by dielectric barrier discharges. J Mater 2009;166:523–30. https://doi.org/10.1016/j.jhazmat.2008.11.068.